Effect of Annealing on Microstructures and Properties of TC4 Heat Dissipation Structure Prepared by LPBF

Kehan Liu[a], Xilin Yao[b], Kaixuan Dongfang[a], Hongju Fan[a], Peng Liu[a]*

[a]Shandong Jianzhu University, School of Materials Science and Engineering, 250101, Jinan, China.
[b]Pennsylvania State University, University Park, USA.

TC4 (Ti6Al4V) alloy is widely used in aerospace, medical equipment, food industry and other fields. Laser powder bed fusion (LPBF) technology has a short production cycle and high precision for formed parts, providing new ideas for the manufacturing of complex structures such as aerospace and having great development prospects and manufacturing advantages. This paper took the TC4 heat dissipation structure prepared by LPBF technology as the study object and established a numerical simulation model to analyze the temperature field changes of the TC4 heat dissipation structure prepared by LPBF. By adopting the annealing heat treatment process, it was found that with the increase in annealing temperature and holding time, the microstructure coarsened, the hardness first increased and then decreased, and the corrosion resistance improved. Among them, when the annealing temperature was 900 °C, and the α' phase was basically transformed into α phase, and the content of β phase increased. The grains and structure of the heat dissipation structure were uniform, and the most significant was in the near inner-pore area. At this point, the hardness value significantly decreased, and the difference in hardness around and outside the heat dissipation hole was 12.42 $HV_{0.2}$.

Keywords: *LPBF, TC4 alloys, microstructure, mechanical properties, annealing.*

1. Introduction

Laser powder bed fusion (LPBF) technology uses a three-dimensional part design model and a high-energy laser beam to melt metal powder. It feeds powder layer by layer along a defined scanning path and solidifies and accumulates, achieving near-net forming of parts[1,2]. Rapid manufacturing, high density of formed parts, good precision, and a high material utilization rate[3] have advantages that traditional forging and casting do not have, providing a new way for the production and manufacturing of complex structural components of titanium alloys with great development prospects[4-6].

TC4 (Ti6Al4V) alloy has the advantages of low density, high specific stiffness, good corrosion resistance, fatigue and creep resistance, and nontoxicity[7,8]. It is widely used in industries such as aerospace, food industry, medical equipment, nuclear power generation, and shipbuilding, and is known as the rising "third metal" and "smart metal"[9]. It is an important strategic metal material, and the application of titanium alloys in aerospace has reached nearly 60% or more[10]. Especially in the past 50 years, the total usage of titanium alloys has continued to steadily increase. Conventional titanium alloy manufacturing often uses casting, forging, and other processes, which have limitations such as high energy consumption, long manufacturing cycles, and low material utilization, which are not conducive to the manufacturing of complex titanium alloy structural components and restrict the application and development of titanium alloys[11].

The components prepared using LPBF technology undergo rapid heating and instantaneous condensation during the production process. The components first expand due to heat and then contract due to cold. Uneven thermal stress accumulates inside the workpiece, which can easily lead to high strength and poor plasticity of the components[12]. At the same time, due to the presence of phase change, the formed components generate structural mismatch internally, leading to phase change stress[13]. Thermal stress and phase transformation stress result in residual stresses that cannot be ignored in the processed components, which can easily lead to cracks, damage, and other phenomena during service, shortening the service life of the components[14]. So post-processing is essential, and due to the limitations of titanium alloy materials, heat treatment has become the current low-cost and most widely used treatment process. Choosing a reasonable heat treatment process can effectively reduce the residual stress caused by sudden cooling during workpiece formation. By adjusting the process, the transformation of α and β phase can be controlled, thereby controlling the size and content of phases, making the microstructure and mechanical properties of the workpiece better match the working environment, and unleashing the potential of titanium alloys[15].

During the heat treatment process, complex TC4 titanium alloy components may exhibit differences in microstructure and grain size in different regions due to the influence of instantaneous temperature and other uncontrollable factors. Therefore, exploring the influence of different heat treatment

processes on the microstructure and properties of TC4 titanium alloy components prepared by LPBF and selecting appropriate heat treatment schemes has certain significance and value for the popularization of LPBF-formed components and the industrial promotion and application of TC4 titanium alloy.

For TC4 samples prepared by LPBF, there is a relatively mature heat treatment process to improve the microstructure and mechanical properties. Liu et al.[16] studied the effect of heat treatment on microstructure and mechanical properties of LPBF TC4 titanium alloy in detail. The results showed that there were a large number of acicular α, α' and β phase in the LPBF TC4 titanium alloy. With the increase in aging treatment temperature, the metastable α' phase of LPBF TC4 decomposed into (α+β) flat noodles. The effect of heat treatment on the microstructure and basic mechanical properties of TC4 alloy was studied in detail. The phase transformation of α and β phase was coarse, and the strength gradually decreased. The plasticity and hardness increased and decreased, respectively. In the solution + aging treatment, the β phase was transformed into α' phase martensite during the solution process, and the aging treatment resulted in the decomposition of the metastable α' phase into (α+β) flat noodles. The strength and hardness of the TC4 alloy increased with increasing temperatures. The best mechanical properties could be obtained by quenching in water at 960 °C for 1 hour and air cooling at 600 °C for 8 hours. Zhou et al.[17] prepared TC4 titanium alloy specimens using the variable parameter forming process (VPFP) of LPBF technology and studied the surface morphology, tensile properties, and microstructure of TC4 titanium alloy specimens. The results showed that in the range of 250-300W laser power, the tensile strength of VPFP was greater than that of the quantitative parameter forming process (QPFP), and the elongation was reduced. By reducing the index of the hierarchical structure, the tensile strength increased to 1190.84 MPa. Compared with the untreated sample, the elongation increased to over 200%, with a maximum elongation of 13%. By increasing the heat treatment temperature, the fracture gradually transformed from a brittle fracture to a ductile fracture, and the microstructure of the specimen gradually changed from a needle-like martensite α' phase to α phase.

In terms of process methods, Waqas et al.[18] studied the density, cross-sectional morphology, microstructure, and mechanical properties of Ti6Al4V alloy parts formed by LPBF before and after heat treatment under laser power, exposure time, and line spacing. The results showed that as the laser power increased, the defects in the parts decreased. In addition, when the laser power was 400W and the exposure time was 30μs, the tensile strength of the part reached 1203 MPa, which was nearly 300 MPa higher than that of ordinary forged Ti6Al4V titanium alloy after annealing. The continuous variation of line spacing within a certain limit (50-65 μm) could increase the relative density to 99.59%, which was much better than the results previously reported. The tensile fracture of the specimen exhibited brittle cracks. Ji et al.[19] investigated the effect of hatch space (HS) on the roughness, fracture morphology, tensile performance, and structural refinement of single layer, top, and side surfaces of LPBF TC4 parts. The results showed that, due to the scanning strategy and stacking effect, the

roughness variation trends of single-layer and block-shaped parts were different. Under optimized process parameters, the total tensile elongation could be further increased to over 15%, while the tensile strength only needs to be increased to 210μm, with an overlap rate of about 23%. After 2 hours of heat treatment at 800 °C, due to the low temperature gradient and solid-state phase transition, the texture was lower and the content of β-phase increased, resulting in the highest total elongation. It led to a decrease in columnar grains and an increase in interfacial spacing and lattice parameters. The fracture mechanism was based on the accumulation of pores generated during the additive manufacturing process.

Domestic and foreign scholars have also conducted relevant research on finite element simulation of different components. Manvatkar et al.[20] simulated the temperature field of thin-walled parts formed by powder-feeding laser-selective melting and analyzed the changes in peak temperature, melt pool width, and cooling rate with the number of forming layers. The results showed that the top area of multi-layer cladding parts had a high temperature, a low cooling rate, and a wider melt pool size. However, the cooling rate of the bottom area of the cladding was faster than that of the top layer, the width of the melt pool was smaller, and the workpiece presented a shape of a wider top and a narrower bottom. Manvatkar et al.[21] established a transient temperature field model for laser near-net forming of thin-walled parts based on the finite element method. In this paper, the variation patterns of the highest temperature and cooling rate of the melt pool were summarized. By studying the relationship between cooling rate and workpiece hardness, the hardness distribution of thin-walled parts was predicted. The lower cooling rate at the top of the workpiece resulted in a decrease in its hardness, while the higher cooling rate at the bottom of the workpiece resulted in a higher hardness. Tavlovich et al.[22] used laser additive manufacturing technology with direct metal deposition to rapidly shape and manufacture complex parts. For the straight-walled model of multi-layer powder deposition, the results showed that the width of the cladding layer can become larger than the width of the melt pool on the substrate surface. An expression for the elongation of the melt pool with increasing lateral velocity was proposed, and the trend of the width and height of the cladding layer was obtained. Moreover, LPBF is a highly dynamic and intricate physical process where individual defects often accumulate into significant internal flaws, subsequently impacting material formation, microstructure, and performance. Addressing potential defects in the LPBF process, Zhang[23] employed real-time monitoring and recording of plume and splashing behaviors through image recognition and tracking. This study elucidated the impact of melt flow evolution on splashing and plume behaviors across three distinct melting modes, introducing a novel method for gathering statistical data on splash-related physical parameters within melting modes. Dai et al.[24] utilized a combined approach of laser shock peening and annealing to fine-tune the microstructure of an additive-manufactured Al-Mg4.5Mn alloy, thereby enhancing its mechanical properties.

Although the aforementioned scholars have conducted research on LPBF-formed components for aviation, the performance of the components they prepared is still unstable

and cannot meet the needs of large-scale industrial production applications. Through in-depth analysis, the main reason for this is the lack of in-depth understanding and exploration of key fundamental issues such as the formation law of internal structure and internal defect formation mechanism, the stress evolution law of parts, and later part processing in laser rapid prototyping of titanium alloy parts both domestically and internationally. This study mainly used TC4 heat dissipation structures prepared by LPBF for aviation as experimental materials. Adopting the annealing heat treatment process, the process parameters will be designed and optimized, which conducting research on differences in different regions of components. Through microscopic and mechanical analysis testing methods, the microstructure, mechanics, and corrosion performance of the TC4 heat dissipation structure near the inner hole and outer side were observed and analyzed. Then, by analyzing the characteristics, a heat treatment process was optimized and established, analyzed and explored the influence mechanism of the heat treatment process on microstructure and performance of different areas of the TC4 heat dissipation structure, and provided an experimental and theoretical basis for the annealing process of LPBF technology to prepare TC4 components.

2. Experimental

2.1. Materials and process methods

This experiment used TC4 titanium alloy powder prepared by the atomization method and formed TC4 aviation radiator components (see Figure 1a) prepared by LPBF technology. The actual components and prepared samples are shown in Figure 1b. The chemical composition (mass fraction, %) of the alloy is shown in Table 1, and the sample size was Φ80 mm × 5 mm. This experiment utilized LPBF-280HL additive manufacturing equipment equipped with an Nb-YAG laser with a rated laser power of 400 W and a scanning speed of 1000 mm/s. The printing work was carried out under an Ar gas protection atmosphere.

Using the method of controlling variables, the changes in the structure and performance of TC4 heat dissipation under different process parameters were explored. Under the condition of air cooling and insulation for 2 hours, an experiment was conducted within the temperature range of 700 °C~1050 °C, with an interval of 50 °C, to explore the effect of different annealing temperatures on the material. Then, the most representative 750 °C/2 h/AC and 900 °C/2 h/AC were selected for the analysis of the internal and external structure of the heat dissipation structure and the discussion of the difference in performance. Under annealing temperatures of 850 °C, 1000 °C, and air-cooling conditions, holding times of 2 hours and 5 hours were selected as experimental variables to explore the effect of different holding times on materials under annealing processes. Finally, 1000 °C/2h/AC and 1000 °C/5h/AC with significant changes were selected for discussion of the differences in microstructure and properties of the internal and external sides of the heat dissipation structure.

2.2. Experiments and characterization methods

A Nikon Epiphoto 300U/200 horizontal metallographic microscope was used to observe the morphology characteristics of alloys. The preparation of metallographic samples mainly included steps such as sampling, embedding, grinding and polishing, corrosion, etc. The metallographic etching solution for LPBF TC4 alloy was Kroll etchant, with a ratio of 3:1:16 for nitric acid: hydrofluoric acid: water. Then, the surface of the sample was corroded for about 25 seconds. The prepared sample surface had no scratches or other impurities, and the metallographic structure of the sample was clear and obvious. Using the Zeiss Gemini SEM300 scanning electron microscope to observe the microstructure around and outside the heat dissipation holes under high magnification, the phase composition through EDS elemental scanning was analyzed. The experimental process includes: the height of the embedded sample to be observed should be less than 5mm; using conductive adhesive to connect the embedded sample to the stage; and sequentially placing multiple
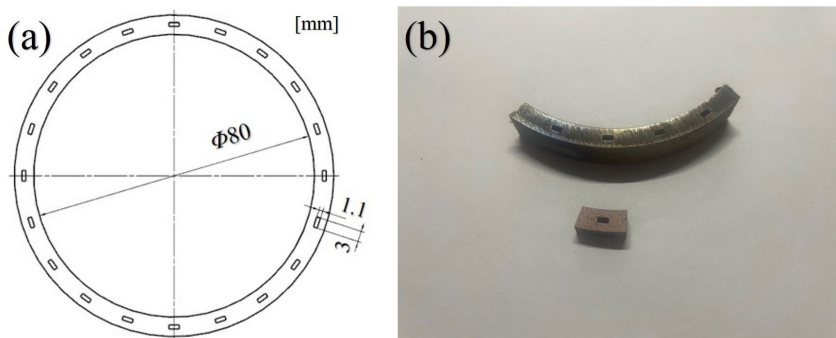
Figure 1. (a) Cross section diagram of TC4 heat dissipation structure prepared by LPBF; (b) Partial heat dissipation structure and schematic diagram.

Table 1. Chemical composition of TC4 alloy (mass fraction, %).

Element	Fe	C	N	Al	V	Ti
Wt.%	0.1	3.3	0.01	2.5	2.2	Bal.

samples to be scanned and analyzed. Before observation, the observation chamber needed to be vacuumed, and then the microstructure of each area of the joint was observed. Performed EDS quantitative analysis on the microstructure of different regions of the heat dissipation structure, combined with SEM analysis of the microstructure.

XRD testing was conducted using a D/max-2500/PC X-ray diffractometer. The equipment parameters were as follows: scanning angle of 20~90 °, step size of 2 °/min, current of 200 mA, acceleration voltage of 40 kV, Cu target and Si powder as internal standards, graphite monochromatic filter.

In hardness testing, a diamond pyramid indenter with a 136°angle opposite the top two phases was pressed into the surface of the specimen using a specified test force. After maintaining the specified time, the test force was removed, and the surface indentation area of the specimen was measured. The Vickers hardness value was the quotient obtained by dividing the experimental force by the indentation area. The equipment used for this hardness measurement was a HV-1000 microhardness tester, which used Vickers hardness to test the experimental samples of TC4 titanium alloy. Each sample was tested for microhardness at 20 points. The test pressure was 0.2 kg, the holding time was 10s, and the step was 500 μm. The actual marking positions are shown in Figure 2a. To avoid measurement errors caused by uneven microstructure, 10 points were taken near the inner hole and outer side of each sample, and the average value was taken. The hardness measurements mentioned below all use this method and will not be repeated. Measure the hardness of heat treatment processes at different annealing temperatures, and the actual spot position is shown in Figure 2b.

Using the CHI-660D electrochemical workstation, electrochemical corrosion tests were conducted on samples of different heat-treated heat dissipation structures to analyze their corrosion resistance performance. The working electrode was a 0.25 mm² TC4 sample; the auxiliary electrode was a platinum electrode; and the reference electrode was a saturated calomel electrode. Using wire cutting to cut corrosion samples after different heat treatments, samples with a size of 10 mm × 5 mm were prepared. The preparation process of electrochemical corrosion specimens included connecting wires to the back of the specimen, immersing the specimen and wires in dissolved paraffin, retaining the

test area on the surface of the specimen, and immersing the wax-sealed specimen in a 3.5% mass fraction NaCl solution. Electrochemical testing parameters: the potential range was relative to the open circuit potential (OCP) ± 200 mV, and the scanning speed was 1 mV/s. The polarization curves and AC impedance of samples with different heat treatment processes were tested separately.

3. Results and Analysis

3.1. Establishment of physical field models

The research object of this work was the heat dissipation structure for aviation, prepared using LPBF technology. The material was TC4 metal powder, which mainly played a role in cooling and increasing the heat dissipation area. For the convenience of observation, the heat dissipation structure was modeled. Figure 3 is a three-dimensional diagram of the heat dissipation structure. After measurement, the inner ring diameter was about 80 mm, the outer ring diameter was about 90mm, the height was 10mm, and the size of the heat dissipation hole was 3 mm × 1.1 mm.

The solid heat transfer equation used in the simulation is:

$$\rho C_p \frac{\partial T}{\partial k} + \rho C_p u \cdot \nabla T + \nabla \cdot q = Q + Q_{ted} \qquad (1)$$

Where ρ is the density of TC4 (kg/m³), C_p is the constant pressure heat capacity of TC4 (J/kg · K), T is the thermodynamic temperature (K), ∇ is the gradient operator, u is the velocity field, the thermal conductivity of k is TC4 (W/m² · K), and Q is the heat (KJ).

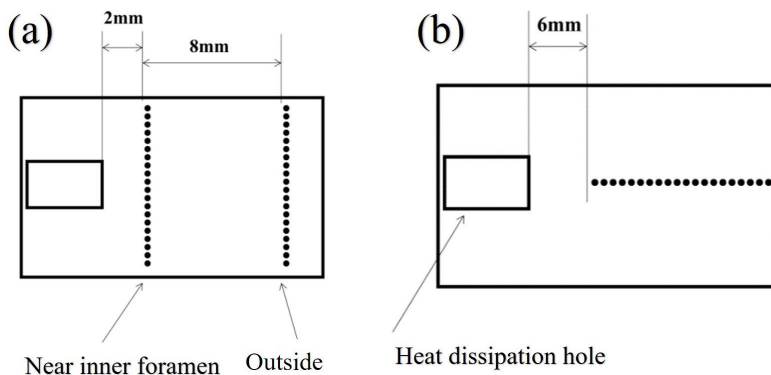$$q = -k\nabla T \qquad (2)$$

Where q is the Fourier thermal conductivity law, k is the thermal conductivity (W · m⁻¹ · K⁻¹), and T is the temperature (K).

The heat source equation used is:

$$-n \cdot q = Q_b \qquad (3)$$

Where n is the normal vector of the boundary surface, and q is the external input heat flux per unit area (J/m²).

Figure 2. Schematic diagram of different hardness measurement location: (a) Along the annular direction of the sample; (b) Perpendicular to the annular direction of the sample.

$$Q_b = \frac{P_b}{A} \qquad (4)$$

Where P_b is pressure drop, A is the cross-sectional area of the heat dissipation structure (m^2).

The initial temperature is 25 °C, and the parameters involved in the simulation, such as elastic modulus, Poisson's ratio, thermal conductivity, and specific heat capacity, are from reference[25]. The specific values are shown in Table 2. Simulate the heat dissipation structure using COMSOL software for different temperature processes. The specific simulation parameters used are shown in Table 3.

In order to improve efficiency and reduce unnecessary workload, an encrypted mapping grid was used in the heat sink area when dividing the grid. A relatively sparse mapping grid was used in the area far from the heat sink on the outside, and a free grid transition was used in the middle. The inner and outer diameters of the heat dissipation structure were relatively small, so the unit size in the heat dissipation hole area was controlled at 0.1 mm × 0.1 mm × 0.1 mm, and the outer unit size was controlled at 0.2 mm × 0.2 mm × 0.2 mm. A total of 37741 units and 8897 grid vertices were generated. The finite element model after partitioning is shown in Figure 4.
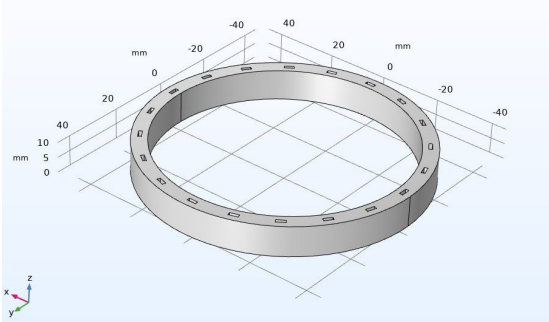

Figure 3. 3D diagram of heat dissipation structure.

The temperature changes in different parts of the heat dissipation structure during the cooling moment of simulated samples at 550 °C, 700 °C, 920 °C, and 1000 °C are shown in Figure 5. In order to further clearly see the temperature changes at different positions, a three-dimensional cross-sectional analysis was selected through the outer side, heat dissipation holes, and inner side to analyze the temperature changes at different positions. The results are shown in Figure 6. From the cloud map, it could be seen that the trend of instantaneous temperature change was the same: the outer side was the first to reach the predetermined temperature, and the heat dissipation structure formed a significant temperature difference on the outer side and near the heat dissipation holes. By selecting the cutoff line shown in Figure 5, further analysis could be conducted on the temperature changes between the outer side, heat dissipation hole, and inner side. It was found that at 550 °C, the temperature difference between the inner and outer sides was small, but as the temperature increased, the temperature difference increased. At the same time, the cooling rate at 1000 °C was better than at 550 °C. There was relevant literature[26] that proved that cooling rate affects grain size. It was speculated that with the change in temperature, the evolution of grain size had certain regularity. The instantaneous temperature on the outer side was greater than that on the inner side, which means that the size of the outer grain may be larger than that on the inner side. The phase transformation products could be varied under different temperatures and cooling times. The material used in this experiment is a TC4 titanium alloy prepared by LPBF, which mainly existed in the densely packed hexagonal α phase and body-centered cubic β phase. The transformation products also varied under different heating treatments and cooling rates[26].

The TC4 heat dissipation structure prepared by LPBF technology had relatively small grains and mainly underwent martensitic transformation, which was also the main part of the solid-state transformation of a dual-phase titanium alloy. According to the crystal structure, martensite was mainly divided into four types: hexagonal martensite,

Table 2. Physical parameters of TC4 alloy[25].

Temperature (°C)	Unit	0	500	700	800	1000
Elastic modulus	[GPa]	112	92	76	56	32
Poisson's ratio	-		0.34	0.37	0.39	0.41	0.42
Yield strength	[MPa]	887	508	212	89	38
Thermal conductivity	[W·m^{-1}·K^{-1}]	6.6	10.3	13.8	14.7	16.9
Specific heat capacity	[J·kg^{-1}·k^{-1}]	606	691	726	736	754

Table 3. Simulation parameter settings.

| Parameter	Number	Unit	Meaning
d_TC4	40	[mm]	Inner diameter of heat dissipation structure
D_TC4	45	[mm]	Outer diameter of heat dissipation structure
H_TC4	10	[mm]	Height of heat dissipation structure
1_TC4	3	[mm]	Length of heat dissipation hole
w_TC4	1.1	[mm]	Width of heat dissipation holes
h_TC4	10	[mm]	Height of heat dissipation hole
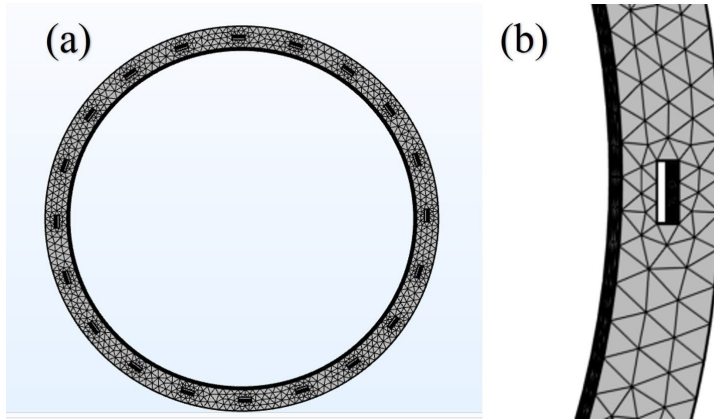
Figure 4. Finite element model after grid partitioning: (a) Overall grid; (b) Local magnification of the grid in the heat dissipation hole area.
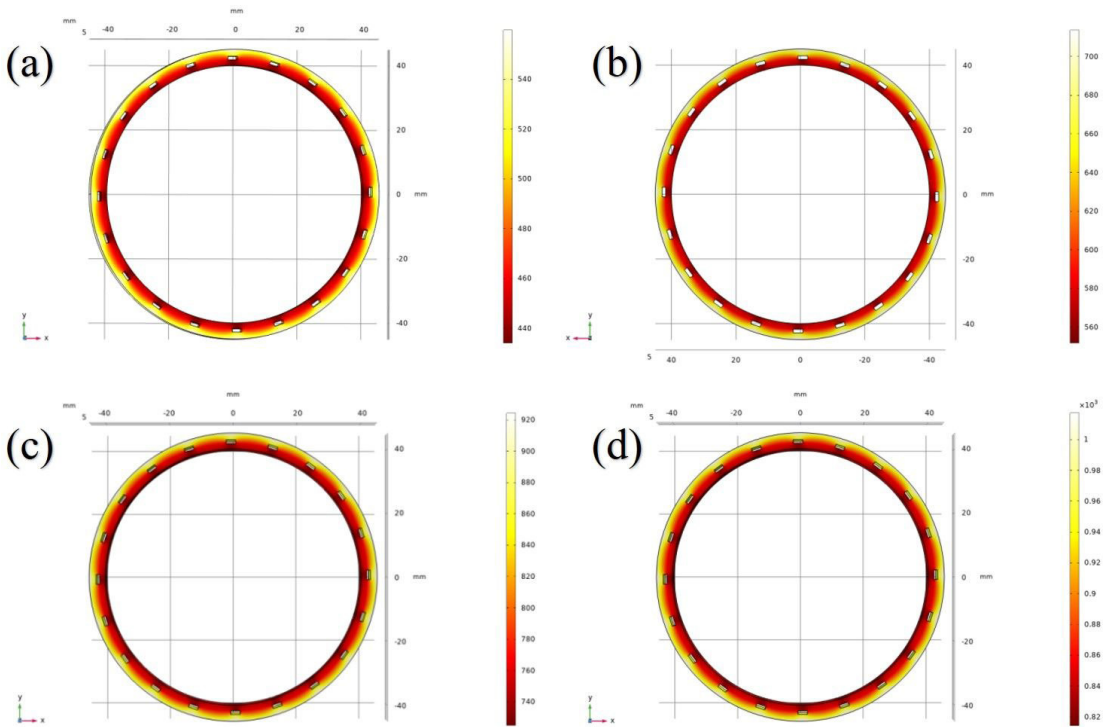
Figure 5. Temperature distribution cloud map under different processes: (a) 550 °C; (b) 700 °C; (c) 920 °C; (d) 1000 °C.

body centered cubic martensite, rhombic martensite, and face-centered cubic martensite. In the preparation of LPBF, hexagonal martensite α' phase and rhombic martensite α'' phase were prone to occur. The hexagonal martensite α' phase appeared in a sheet-like shape without twinning inside, while the rhombic martensite α'' phase appeared in a needle-like shape with possible twinning inside. In the microstructure of TC4, owing to the extremely high cooling rate of the LPBF process, very fine needle-like martensite α' with minor β and α'' structures is formed. Microstructural observations confirm that the fine needle-like martensite

α' fully decomposes in the post-heat treatment cycle, transforming into α, β, and α'' phases, and generating some nanoscale β particles during the cooling stage, thereby necessitating post-treatment for the TC4 alloy following LPBF fabrication[27]. Martensite is a metastable phase that decomposes into a stable phase with increasing temperature during heat treatment. The α' phase could be directly decomposed into α' phase, which underwent a transition phase. In addition, the formation conditions of martensite were also influenced by the elemental composition and content of titanium alloys, as well as the heat treatment
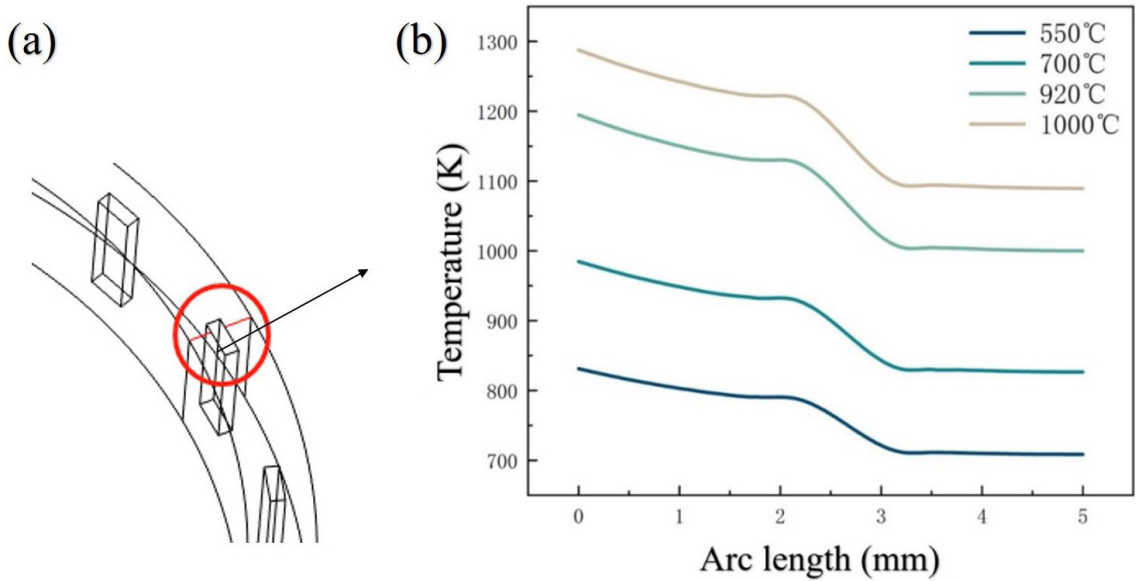
Figure 6. Cutting position and temperature changes curve of TC4 samples: (a) The cutting position of sample; (b) Temperature changes curve for TC4 samples.

process, especially the instantaneous temperature changes after heat treatment, which were closely related. Therefore, further experimental analysis and verification is needed for the specific phase transformation and microstructure evolution.

3.2. Microstructures

Figure 7 shows the microstructure morphology at forged, As-build and 700~1050 °C state, maintained at a constant temperature for 2 hours, and cooled to room temperature with air. The microstructure of the TC4 specimen in forged state was composed of coarse equiaxed (α+β) phases, with the primary α phase mainly being ellipsoidal and short rod-shaped. The microstructure was relatively uniform, and no gradual change was observed. Different from the microstructure of forged samples, TC4 samples prepared by LPBF technology had a short laser action time and fast cooling rate, and the microstructure was composed of fine needle like martensite α' phase and a small amount of β phase. When the annealing temperature was 700~800 °C, the microstructure was a clear, layered structure composed of secondary α phase and a small amount of β phase. With the increase in annealing temperature, the layered structure gradually decomposed, and the β phase was clearly visible. At 850 °C, the secondary α phase had transformed into various forms of α phase, and there were obvious structural differences in the near inner and outer sides of the heat dissipation structure: the near inner-pore area was mainly composed of α "clusters" with tightly arranged grains and smaller sizes. The outer tissues appeared to be spherical, rod-shaped, flat noodles, and other forms of α phase, which were loosely arranged and anisotropic.

When the annealing temperature was 900~1050 °C, the structure was dominated by (α+β) phase, and the β phase was clearly visible. The grain size increased slightly compared with the annealing temperature of 850 °C, and

the morphology changed little. The structure near the inner hole also had a variety of α phase morphologies, such as spherical and flat-noodle-shaped. The grains grew around the edge of the heat dissipation hole, and the arrangement was relatively loose. The pattern obtained from annealing samples at different temperatures was as follows: with the increase in annealing temperature, the transformation from secondary α phase to α phase occurred, the content of β phase increased, various forms of α phase appeared, the grain size increased, and the difference in microstructure between the inner and outer sides of the heat dissipation structure increased.

To further observe the differences in the near inner pore and outer microstructure of TC4 prepared by LPBF, annealing processes at 750 °C and 900 °C with significant tissue changes were selected. After roughly distinguishing between the near inner pore and the outer microstructure, scanning electron microscopy was used for further observation. The analysis is as follows.

Figure 8 shows the microstructure of LPBF heat dissipation structure at 750 °C and 900 °C, maintained at a constant temperature for 2 hours, and cooled to room temperature with air. As shown in Figure 8, when the temperature was 750 °C, the microstructure of the heat dissipation structure was not significantly different from the as-build state, and it was needle-like martensite α' phase and (α+β) phase. The distinction between the inner foramen and the outer side was not clear, and there were many layered tissues on the outer side. As the heat treatment temperature increased, α' phase gradually decomposed into α phase, while β phase was scattered in α phase and its content increased. When the temperature was 900 °C, α phase grew from fine needle to coarse lath and spherical, while the grain boundary of β phase was clearly visible. By comparing the area around the heat dissipation hole, it can be observed that the grains and structure around the inner hole of the heat dissipation
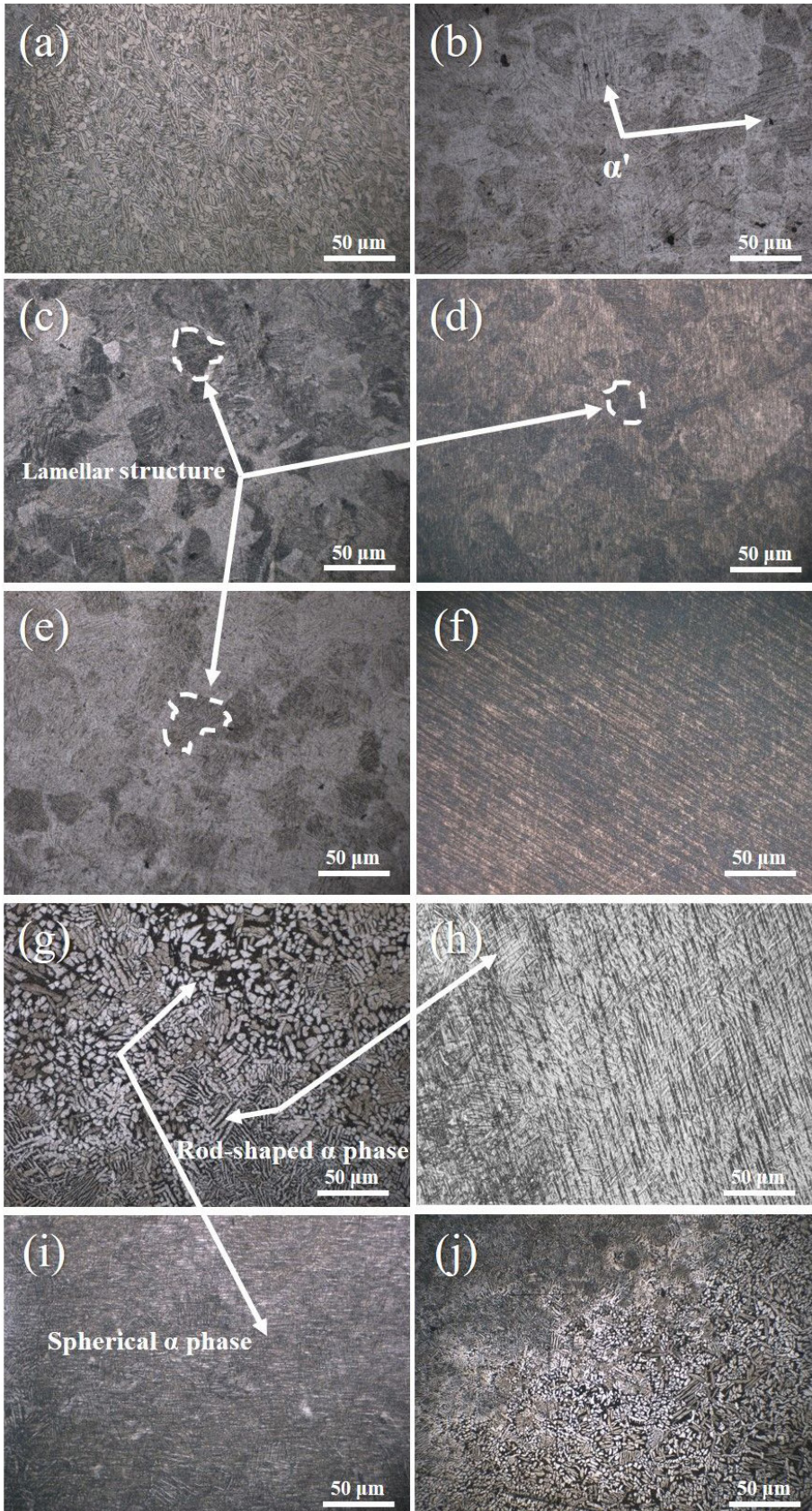
Figure 7. Preparation of TC4 samples at different states: (a) forge; (b) LPBF; (c) 700 °C; (d) 750 °C; (e) 800 °C; (f) 850 °C; (g) 900 °C; (h) 950 °C; (i) 1000 °C; (j) 1050 °C; (c-j) Different annealing temperatures by LPBF.

component were more uniform. This was because the area around the heat dissipation hole was the first to receive heat, resulting in a higher degree of heat accumulation and a faster heat dissipation rate compared to the external position.

In order to further explore the microstructure transformation of the heat dissipation structure of LPBF-formed TC4 under different annealing temperatures, SEM was used for analysis. Figure 9 and Figure 10 show the microstructure near the inner and outer pores of the heat dissipation structure at 750 °C and 900 °C, respectively. According to Figures 11a and 11b, it could be seen that when the annealing temperature reaches 750 °C, the size of the needle-shaped α' phase increases compared

to the untreated sample, and it is short and disorderly with no directionality in distribution. The distribution of β phase was spherical and scattered, with an extremely low content. Near the inner pore, α' phase intersected and was more numerous than the outer one, while the protruding α' phase on the outer side decreased and a layered α phase appeared.

It can be seen from Figs. 10a and b that when the annealing temperature reached 900 °C, the acicular martensite α' phase transformed into the fractured coarse lath α phase, which may be caused by the following factors: The flat noodle α phase would truncate the grain boundary α phase during the growth process[28]. At the same time, the dislocation rearrangement

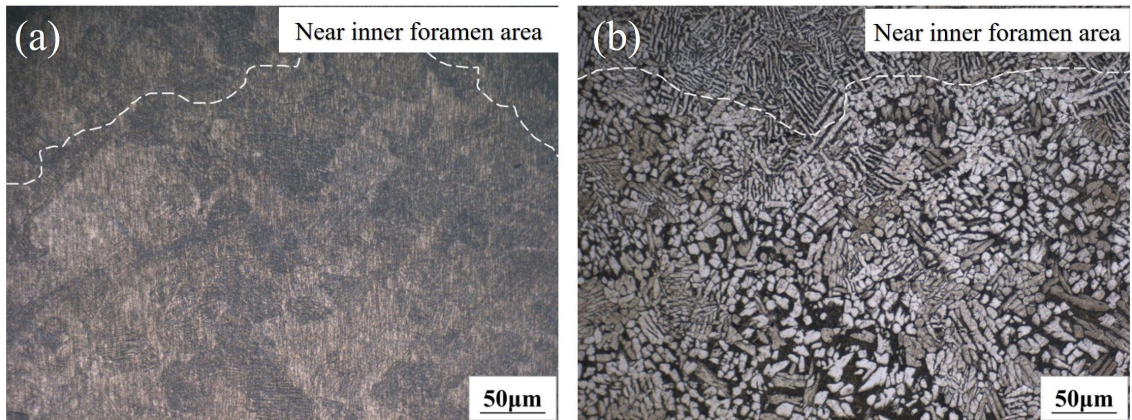**Figure 8.** LPBF TC4 annealing samples: (a) 750 °C; (b) 900 °C.
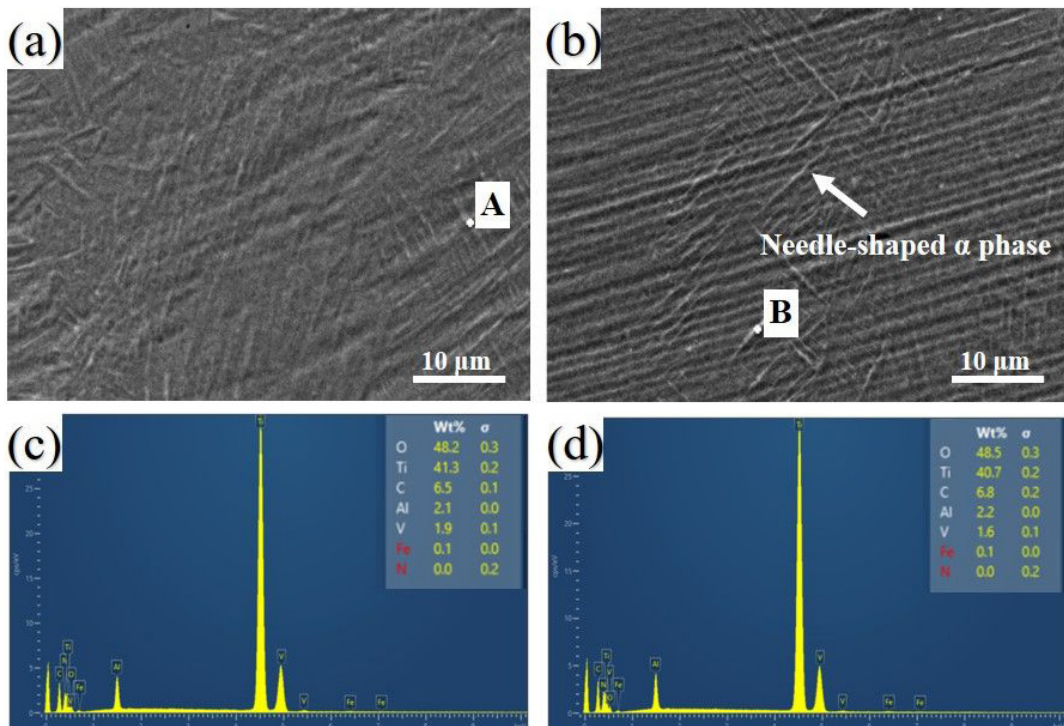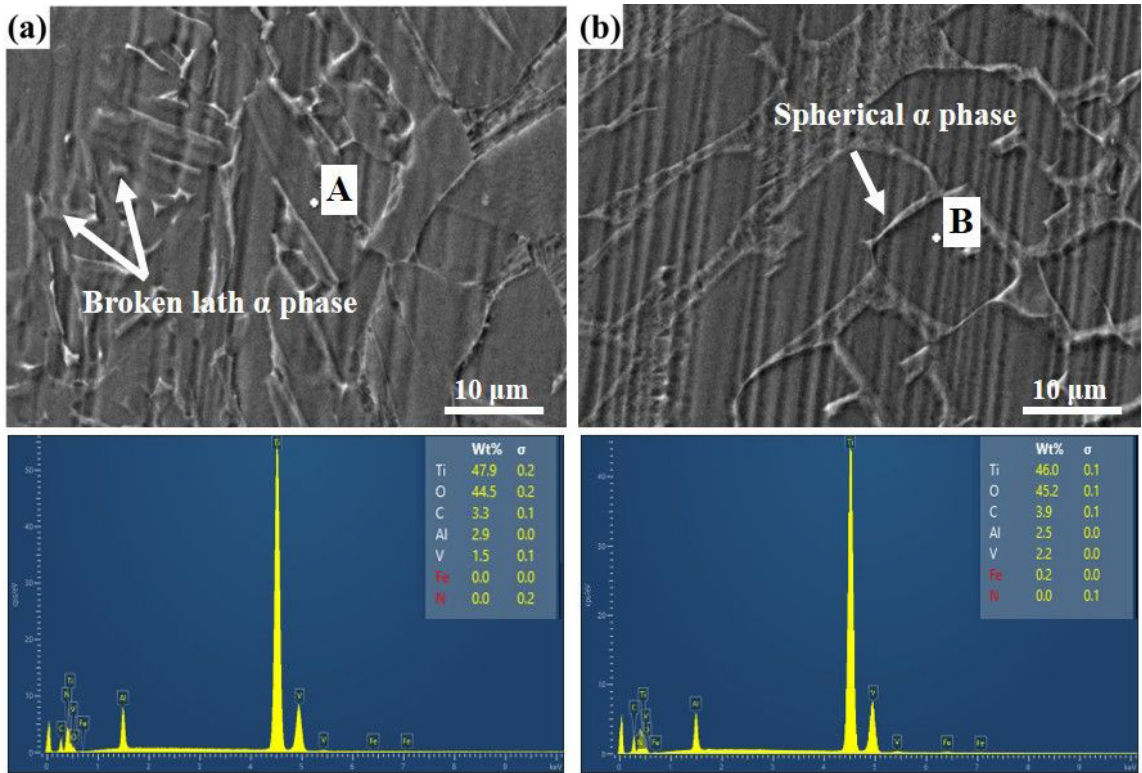

Figure 9. SEM morphology and EDS analysis of TC4 prepared by LPBF under 750 °C annealing process: (a) Proximal foramen; (b) Lateral; (c) EDS analysis in zone A; (d) EDS analysis in zone B.

Figure 10. SEM morphology and EDS analysis of TC4 prepared by LPBF under 900 °C annealing process: (a) Proximal foramen; (b) Lateral; (c) EDS analysis in zone A; (d) EDS analysis in zone B.

formed a plane dislocation array, and a subgrain boundary was formed during the heat preservation process. The existence of the subgrain boundary made α phase of the flat noodles fracture. In addition, near the inner hole, due to the initial heating and relatively high temperature, part of the flat noodles in α phase broke, and a small amount of equiaxed α phase (grains with a small size difference in each direction) was generated at the grain boundary. The lath and spherical α phases at the outer side were relatively intact, and the boundaries between α phase and α phase were obvious. The grain size was slightly larger than that near the inner hole. Analysis of the EDS graph revealed that at an annealing temperature of 750 °C, the needle-like martensite α' phase near the inner and outer pores was composed of elements such as O, Ti, C, Al, V, Fe, etc. Compared with the as-build state, the content of O elements on both the inner and outer sides increased. It was speculated that this may be due to the increase in the size of the secondary α phase, which adsorbed more O elements to form oxides. At 900 °C annealing temperature, two different forms of α phase were analyzed. Near the inner hole area, the fractured lath α phase was analyzed. It was found that at this time, the proportion of Ti elements was the largest, reaching 47.9%. On the outside, the composition of the spherical α phase was analyzed, and at this time, the proportion of the Ti element was 46%. In summary, as the annealing temperature increased, the content of Ti atoms in α phase continuously increased and was not affected by the grain morphology.

Figure 11a shows the XRD patterns at different annealing temperatures. Through analysis, it was found that the diffraction peak representing the β phase in the as-build state was not displayed due to its extremely low or non-existent content. As the annealing temperature increased, the intensity of the diffraction peak representing the β phase continued to increase. The diffraction peaks in the as-build state and annealing processes at 700 °C and 750 °C were mainly α' phase. A diffraction peak of α phase appeared at 800 °C, and the intensity of the diffraction peak gradually increased. When the annealing temperature reached 850 °C, no diffraction peak characterizing α' phase was detected. Combined with metallographic analysis, it was believed that with the increase in annealing temperature, α' phase transformed into α phase. Further phase analysis was performed on XRD annealed at 750 °C and 900 °C to determine other diffraction peaks. Figure 11b shows the X-ray diffraction spectra under annealing treatment at 750 °C and 900 °C in the as-build state. Combined with SEM, it could be seen that the TC4 heat dissipation structure prepared by LPBF consists of α' phase and very little β phase. The detected diffraction peaks were (100) α'-Ti, (002) α'-Ti, (101) α'-Ti, (102) α'-Ti, (110) α'-Ti, (112) α'-Ti, (201) α'-Ti, and (211) β-Ti. Combining SEM and metallographic analysis, it was found that after annealing treatment, as the heating temperature increased, the α' phase gradually transformed into the (α+β) phase. The crystal structures of α' phase and α phase were the same, and their positions in the diffraction pattern were
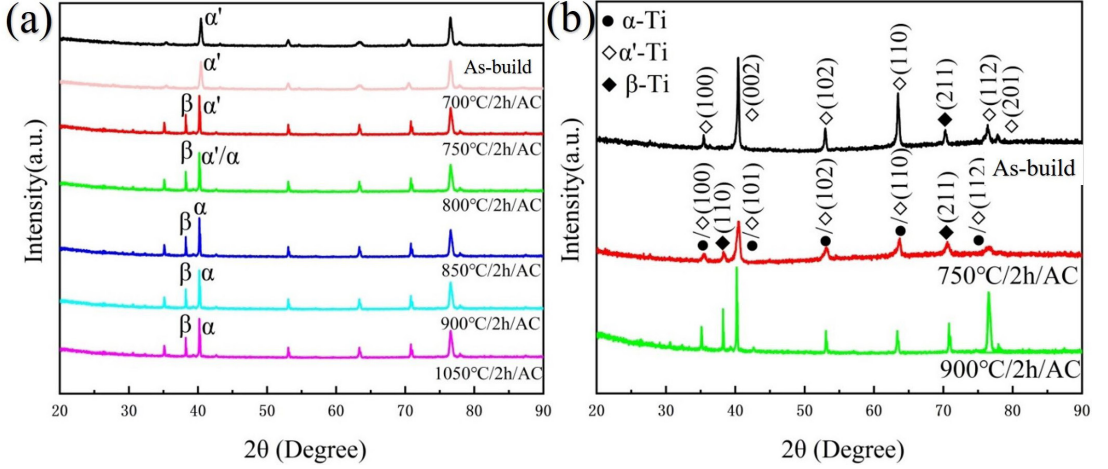
Figure 11. XRD characterization of LPBF TC4 samples: (a) Different annealing temperatures; (b) magnified image.

the same[24]. The main diffraction peaks detected were (100) α'/α-Ti, (101) α'/α-Ti, (102) α'α-Ti, (110) α'α-Ti, (112) α'α-Ti, and (110) β-Ti, (211) β-Ti. By comparing the diffraction peaks of the original and annealed states, the phase diagram of the alloy showed that under the annealing process, as the temperature increased, the α' phase decomposed, the grain size increased, and the β phase content increased. Among them, the grain size of phase A and the content of β phase at 900 °C were significantly higher than those at 750 °C. Through XRD, it can be seen that the diffraction peak of α' phase narrowed and the half width of the diffraction peak decreased at 900 °C. The relationship between grain size and the half width of the diffraction peak can be obtained through Scherrer's formula[29]. The average grain size of α phase was inversely proportional to the half width, so the grain size increased with the increase in annealing temperature.

$$D = \frac{K\lambda}{\beta\cos\theta} \qquad (5)$$

where D is grain size, β is Half peak width, κ is constant (usually 1), λ is X-ray wavelength, θ is Cape Prague.
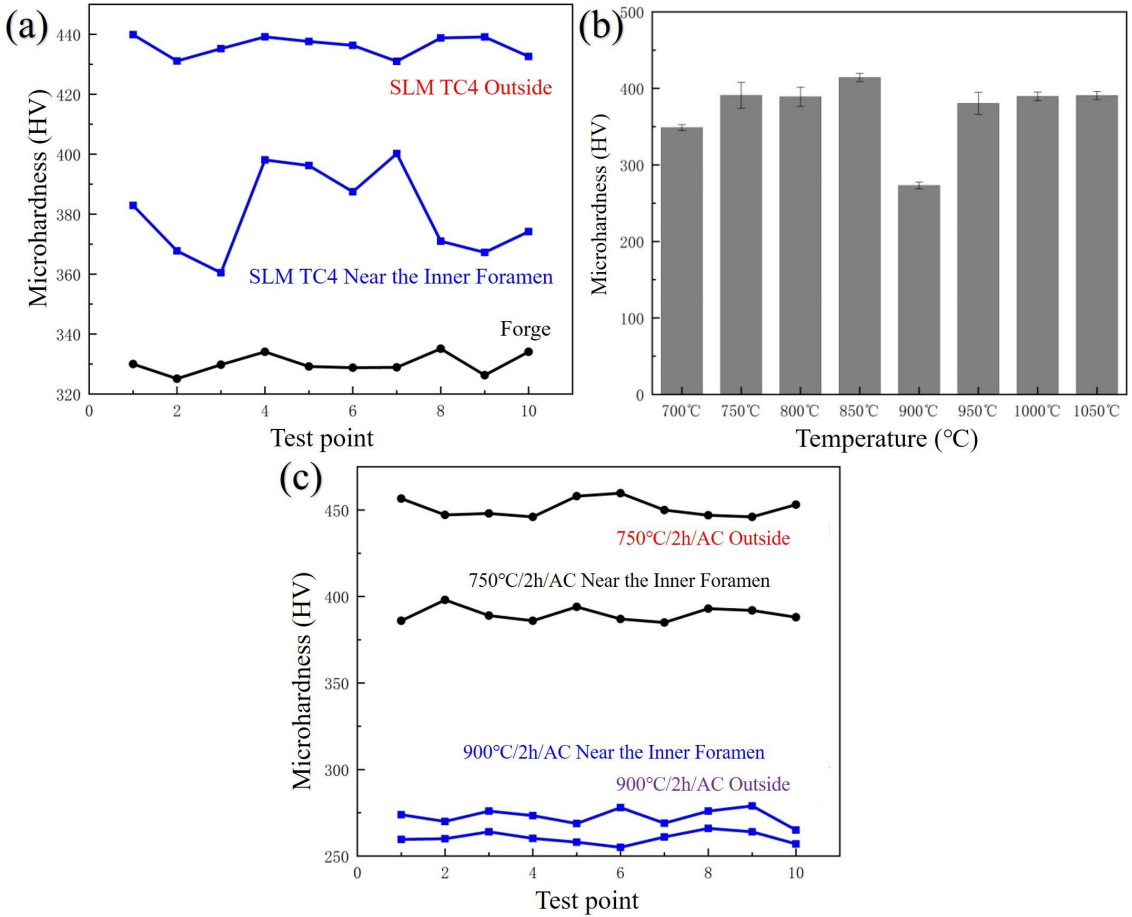
3.3. Microhardness

In order to further analyze the difference in mechanical properties between the forged state and the LPBF-prepared heat dissipation structure near the inner hole and outer side, micro-Vickers hardness was used for testing. The test results are shown in Figure 12a, and it can be seen that the hardness of the forged TC4 titanium alloy was relatively uniform, with an average value of $330.142 HV_{0.2}$. The original TC4 prepared by LPBF had an average hardness value of $380.552 HV_{0.2}$ near the inner hole and $436.075 HV_{0.2}$ on the outer side, respectively. Among them, during the measurement of TC4 in its as-build state near the inner hole, it was found that the numerical changes were relatively large. Based on the microstructure, it may be due to the presence of a large number of "clusters" composed of sheet-like α' phases in the near inner hole area, with the dot position precisely on the "clusters". The internal and external hardness of the as-build state was higher than that of the forged state because the as-build state structure was mainly composed of needle-like martensite α' phase, while the forged state structure was mainly composed of α phase. The needle-like martensite α' phase was a supersaturated solid solution with lattice distortion, and the hardness is much higher than that of α phase[28].

Measure the hardness and calculate the average value, as shown in Figure 12b. As the annealing temperature increased, the overall hardness showed a trend of first increasing, then decreasing, and then slowly increasing again. Among them, the hardness at 750 °C annealing temperature was slightly higher than that at 800 °C annealing temperature, and the hardness of the sample at 900 °C annealing temperature was lower than that in the as-build state and other annealing processes. Combined with metallographic and XRD analysis, this was because, as the annealing temperature increased, the secondary α phase in the structure gradually transformed into α phase. According to relevant literature, the hardness of secondary α phase was the highest, followed by α phase and β phase. At 700 °C, although the organization was mainly composed of secondary α phases, the content was relatively low, resulting in low hardness. As the temperature increased, the size and content of secondary α phase increased, indicating an increase in hardness. At 900 °C, almost all of the secondary α phase was transformed into α phase, and some α phases were affected by temperature to fracture. At the same time, the content of β phase increased, which affected the overall average hardness value, resulting in lower process hardness at this temperature. The hardness of the samples at temperatures ranging from 950 °C to 1050 °C was not significantly different. This was because the growth rates of the generated α phase size slowed down at this time while the content of β phase increased.

Further analyze the hardness under the annealing processes of 750 °C and 900 °C, use the actual measurement positions mentioned in Figure 12c to mark the near inner hole and outside of these two annealing temperature processes separately, and record the hardness values. Figure 13 shows the internal and external hardness changes

Figure 12. Microhardness of LPBF TC4 alloy: (a) As-build and forged state; (b) Different annealing temperatures; (c) annealing samples at 750 °C and 900 °C.
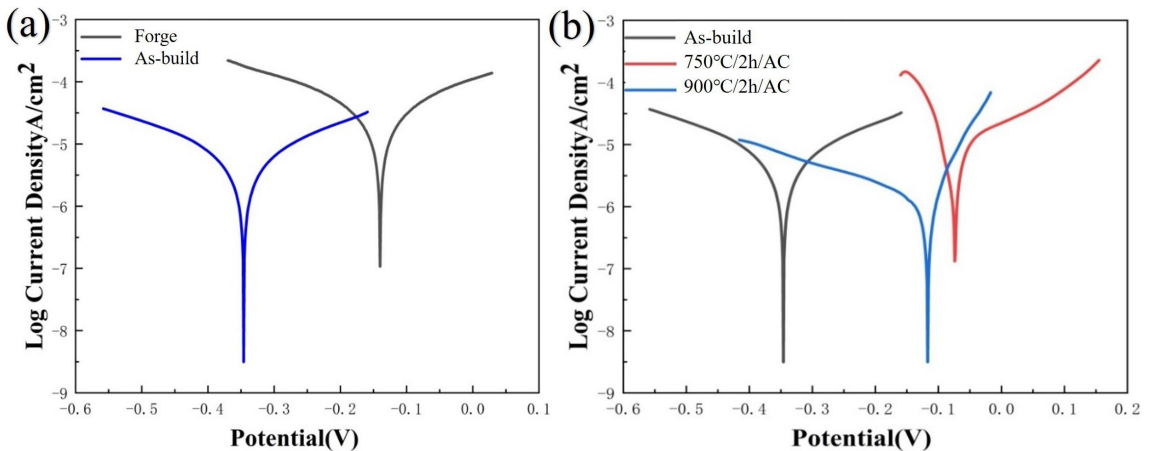
Figure 13. Polarization curve: (a) As-build and forged state; (b) As-build and annealing state.

of the heat dissipation structure under annealing processes at 750 °C and 900 °C. The internal and external hardness under the 750 °C/2 h/AC process was 389.8 HV$_{0.2}$ and 451.16 HV$_{0.2}$, respectively. The internal and external hardness under the 900 °C/2 h/AC process was 272.901 HV$_{0.2}$ and 260.481 HV$_{0.2}$, respectively. At 750 °C, the hardness of

both the inner and outer sides was higher than the as-build state. Based on metallographic analysis, it was speculated that this may be due to the growth of grains with increasing temperature, which generated a large amount of needle-like martensite α' phase at 750 °C, and the content of the inner side was lower than that of the outer side, resulting in lower hardness near the inner hole and higher hardness on both the inner and outer sides than the as-build state. At 900 °C, the internal and external hardness was lower than that of the as-build state because the acicular martensite α' phase was transformed into a lath and spherical α phase with the increase in temperature and coarsens, resulting in internal dislocation stress[30]. The grain size of α phase near the inner hole was lower than that of the outer side, and the content of β phase increased slightly compared to 750 °C, while the content of β phase near the inner hole was higher than that of the outer side. Because the hardness of β phase was lower than that of α phase and α' phase[31], the hardness on the outer side was lower than that near the inner hole at 900 °C.

3.4. Electrochemical corrosion

In order to investigate the effect of LPBF and different annealing processes on the corrosion resistance of TC4 alloy, electrochemical corrosion tests were conducted. Polarization is a phenomenon where static current flows through the electrode and the potential deviates. The polarization curve reflects the relationship between potential and current/density, and by judging the polarization curve, passivation and corrosion can be obtained. Corrosion potential and corrosion current density are two important factors that characterize the corrosion resistance of materials: corrosion potential reflects the dissolution process of materials, and the smaller the current and the less material dissolution, the more corrosion-resistant the material is[31]. The corrosion current density is manifested as the corrosion rate of the material, and the higher the corrosion current density, the greater the corrosion rate. In addition, when titanium alloys are exposed to air, they are prone to adsorbing oxygen-containing particles on the surface, forming a dense oxide film that causes passivation. Therefore, to determine the corrosiveness of titanium alloys, it is necessary to consider the corrosion potential at the beginning of passivation comprehensively.

Figure 13a shows the relationship between corrosion current density and corrosion voltage in the forged and as-build states. The relevant electrochemical parameters are shown in Table 4. It could be seen that both the forged and LPBF-prepared TC4 alloys exhibited metal passivation curve characteristics, resulting in the passivation phenomenon. When the potential of the forged sample reached around -0.13 V, a plateau appeared on the curve, indicating the appearance of a passivation film on the surface of the sample. When the potential reached around -0.1 V, the corrosion current increased, indicating that the passivation film on the surface of the sample was destroyed and the reaction rate increased. When the potential reached around 0.1 volts, The growth rate of the corrosion current was slow, and it was speculated that the formation of a new passivation film at this time would reduce the reaction rate. The TC4 as-build state sample prepared by LPBF exhibited a passivation phenomenon at around -0.37V.

By comparing the forged state with the as-build state, it was found that the corrosion potential in the forged state was -0.14 V, which was higher than that in the as-build state, indicating that the forged sample was less prone to corrosion. At the same time, the polarization curve of the as-build state prepared by LPBF was located below the forged state, indicating that when the potential was the same, the corrosion current density in the as-build state was smaller and more corrosion-resistant.

Figure 13b shows the relationship between corrosion current density and corrosion voltage in the as-build state and heat treatment. The relevant electrochemical parameters are shown in Table 4. By comparing the as-build state, it could be seen that the corrosion potential of the samples treated with annealing at 750 °C and 900 °C was higher than that of the as-build state, indicating that the samples were less prone to corrosion after annealing. Among them, the corrosion resistance under annealing at 900 °C was better than that of the as-build state. Based on metallographic analysis, it was speculated that the presence of a large amount of α' and β phases in the as-build state was the reason for the deterioration of electrochemical performance, and the uneven layered structure led to an uneven and dense passivation film[32]. Compared to the annealing process at 900 °C, the corrosion resistance of the α' phase in the structure was slightly lower at 750 °C due to the lower annealing temperature, and the α' phase was not fully transformed into α phase. As the annealing temperature increased, α' phase transformed into α phase, and the microstructure was mainly composed of (α+β) phase. The disappearance of layered structure and grain growth made the microstructure more uniform, resulting in a denser passive film and improved corrosiveness.

In summary, regarding electrochemical corrosion resistance, the TC4 alloy fabricated by LPBF process was more susceptible to corrosion than its forged counterpart, with annealing further aggravating this issue. However, as the annealing temperature rose, corrosion resistance improved. Microhardness showed the opposite trend. The average microhardness of the LPBF specimens was higher than that of the forged specimens. Following annealing, the average microhardness of the LPBF-prepared samples initially increased and then significantly decreased.

Table 4. TC4 electrochemical corrosion test results.

Process	Corrosion potential (V)	Corrosion current density (A/cm²)	Corrosion potentiometer (V)
Forge	-0.14	3.211×10^{-7}	-0.13
As-build	-0.346	5.751×10^{-7}	-0.33
750°C/2h/AC	-0.074	1.292×10^{-5}	-0.05
900°C/2h/AC	-0.117	1.422×10^{-6}	-0.1

4. Conclusions

The TC4 alloy heat dissipation structure prepared by LPBF was analyzed using the controlled variable method and different annealing processes. The main research content included the differences in microstructure and hardness properties in different regions of the heat dissipation structure, XRD phase analysis, and electrochemical performance analysis. The following conclusions were obtained:

(1) By establishing a numerical simulation model, the temperature field changes of the TC4 heat dissipation structure prepared by LPBF were analyzed. The instantaneous temperature changes of the heat dissipation structure passing through the outer side, heat dissipation holes, and inner side were measured. At the same time, it provided temperature change parameters and the basis for subsequent experiments, facilitating specific research on microstructure evolution and grain growth laws.

(2) The TC4 prepared by LPBF was different from the forged TC4, with a microstructure composed of a small α' phase and a small amount of β phase. The near inner pore region was mainly composed of α' phase clusters, while the outer region was mainly composed of slender and randomly distributed α phases. With the increase in annealing temperature, α' phase gradually decomposed into α phase, and the grains grew continuously, appearing spherical, short rod, flat noodles, and other forms. The α phase near the inner hole area was greatly affected by temperature, resulting in grain fracture. The volume fraction of β phase continued to increase, with rapid growth occurring between 700 °C and 900 °C and slowed growth occurring between 900 °C and 1000 °C.

(3) The hardness of TC4 prepared by LPBF was about 50 $HV_{0.2}$ higher than that of the forged state, and the hardness distribution on the surface of the sample was uneven, with the outer side having a higher hardness than the inner side. After annealing treatment, the hardness of the inner and outer sides showed a trend of first increasing and then decreasing: at 750 °C~900 °C, the hardness increased slightly, and the hardness of the outer side was greater than that of the inner side. At 900 °C, the grains within the organization fractured, resulting in a hardness of about 100 $HV_{0.2}$ lower than the as-build state. At 900 °C~1050 °C, the broken grains grew, the hardness increased, and the values were closer to the as-build state.

(4) The electrochemical performance of TC4 prepared by LPBF was not significantly different from that of TC4 in the forged state: TC4 in the forged state was less prone to corrosion, while TC4 prepared by LPBF was more corrosion-resistant. The composition of the internal phase of the organization was the main reason affecting its electrochemical performance. The uneven distribution of the α' phase prevented the formation of a dense passivation film on the surface of the workpiece, resulting in weak corrosiveness. The large size and uniformly dispersed (α+β) phase of α phase were conducive to the formation of passivation film and hindered the progress of corrosion. Therefore, as the annealing temperature increased, the electrochemical performance improved.

5. Acknowledgments

6. References

1. Fan HJ, Xu YL, Li HX, Fang JY, Li MX, Dongfang KX, et al. A novel study on microstructure and crystallographic characteristics of Cu-Cr-Zr alloy manufactured by laser powder bed fusion. Mater Today Commun. 2023;37:107603.

2. Wang Y, Guo W, Xie YK, Li HX, Zeng CY, Xu M, et al. In-situ monitoring plume, spattering behavior and revealing their relationship with melt flow in laser powder bed fusion of nickel-based superalloy. J Mater Sci Technol. 2024;177:44-58.

3. Rafi HK, Starr TL, Stucker BE. A comparison of the tensile, fatigue, and fracture behavior of Ti-6Al-4V and 15-5 PH stainless steel parts made by selective laser melting. Int J Adv Manuf Technol. 2013;69:1299-309.

4. Vaithilingam J, Goodridge RD, Hague RJM, Christie SDR, Edmondson S. The effect of laser remelting on the surface chemistry of Ti6al4V components fabricated by selective laser melting. J Mater Process Technol. 2016;232:1-8.

5. Mullen L, Stamp RC, Fox P, Jones E, Ngo C, Sutcliffe CJ. Selective laser melting: a unit cell approach for the manufacture of porous, titanium, bone in-growth constructs, suitable for orthopedic applications. II. Randomized structures. J Biomed Mater Res B Appl Biomater. 2010;92:178-88.

6. Fan HJ, Hu JY, Wang Y, Zhang HQ, Guo W, Li JS, et al. A review of laser additive manufacturing of high-strength aluminum alloy: methods, microstructure and mechanical property. Opt Laser Technol. 2024;175:110722.

7. Rezvanian P, Daza R, López PA, Ramos M, González-Nieto D, Elices M, et al. Enhanced biological response of AVS-functionalized Ti6Al4V alloy through covalent immobilization of collagen. Sci Rep. 2018;8:3337-48.

8. Todaro CJ, Easton MA, Qiu D, Zhang D, Bermingham MJ, Liu EW, et al. Grain structure control during metal 3D printing by high-intensity ultrasound. Nat Commun. 2020;11:142-8.

9. Tan XP, Kok YH, Toh WQ, Tan YJ, Descoins M, Mangelinck D, et al. Revealing martensitic transformation and α/β interface evolution in electron beam melting three-dimensional-printed Ti6Al4V. Sci Rep. 2016;6:26039.

10. Xu M, Li, HX, Liu Q, Shan FH, Zhang YX, Guo W. In situ tensile observation of the effect of annealing on fracture behavior of laser additive manufactured titanium alloy. Materials. 2023;16:3973.

11. Olakanmi EO, Cochrane RF, Dalgarno KW. A review on selective laser sintering/melting (SLS/SLM) of aluminium alloy powders: processing, microstructure, and properties. Prog Mater Sci. 2015;74:401-77.

12. Campanelli SL, Casalino G, Contuzzi N, Ludovico AD. Taguchi optimization of the surface finish obtained by laser ablation on selective laser molten steel parts. Procedia CIRP. 2013;12:462-7.

13. Kruth JP, Levy G, Klocke F, Childs THC. Consolidation phenomena in laser and powder-bed based layered manufacturing. CIRP Ann. 2007;56:730-59.

14. Shakil SI, Smith NR, Yoder SP, Ross BE, Alvarado DJ, Hadadzadeh A, et al. Post fabrication thermomechanical processing of additive manufactured metals: a review. J Manuf Process. 2022;73:757-90.

15. Ahn DG. Direct metal additive manufacturing processes and their sustainable applications for green technology: a review. International Journal of Precision Engineering and Manufacturing-Green Technology. 2016;3:381-95.

16. Liu XH, Cui W, Wang YR, Liu FL, Liu YJ. Effects of heat treatment on the microstructure evolution and mechanical properties of selective laser melted TC4 Titanium alloy. Metals (Basel). 2022;12:702-18.

17. Zhou YS, Liu Y, Sun XH, Shi WT, Han YF, Li JH, et al. Effect of heat treatment on the formed specimen of TC4 titanium alloy by selective laser melting variable parameter forming process. Appl Phys, A Mater Sci Process. 2022;128:917-23.

18. Waqas M, He D, Liu Y, Riaz S, Afzal F. Effect of heat treatment on microstructure and mechanical properties of ti6al4v alloy fabricated by selective laser melting. J Mater Eng Perform. 2022;32:680-94.

19. Ji LN, Wang S, Wang CZ, Zhang YB. Effect of hatch space on morphology and tensile property of laser powder bed fusion of Ti6Al4V. Opt Laser Technol. 2022;150:107929.

20. Manvatkar V, De A, Debroy T. Spatial variation of melt pool geometry, peak temperature and solidification parameters during laser assisted additive manufacturing process. Mater Sci Technol. 2015;31:924-30.

21. Manvatkar VD, Gokhale AA, Reddy GJ, Venkataramana AA. Estimation of melt pool dimensions, thermal cycle, and hardness distribution in the laser-engineered net shaping process of austenitic stainless steel. Metall Mater Trans, A Phys Metall Mater Sci. 2011;42:4080-7.

22. Tavlovich B, Shirizly A, Katz R. EBW and LBW of additive manufactured Ti6Al4V products. Weld J. 2018;97:179-90.

23. Zhang YX, Guo W, Shi JX, Chi JX, Chen GX, Han GF, et al. Improved rotating bending fatigue performance of laser directed energy deposited Ti6Al4V alloys by laser shock peening. J Alloys Compd. 2024;980:173664.

24. Dai W, Guo W, Xiao J, Zhu Y, Qi ZW, Shi JX, et al. Tailoring properties of directed energy deposited Al-Mg alloy by balancing laser shock peening and heat treatment. J Mater Sci Technol. 2024;203:78-96.

25. Zhou ZF. Research on Hot Sizing Technology of TC4 Titanium Alloy [dissertation]. Nanjing: Nanjing University of Aeronautics and Astronautics; 2009. (in Chinese).

26. Shahriyari F, Razaghian A, Taghiabadi R, Peirovi A, Amini A. Effect of friction hardening pre-treatment on increasing cytocompatibility of alkali heat-treated Ti6Al4V alloy. Surf Coat Tech. 2018;353:148-57.

27. Jaber H, Kónya J, Kulcsár K, Kovács T. Effects of Annealing and Solution Treatments on the Microstructure and Mechanical Properties of Ti6Al4V Manufactured by Selective Laser Melting. Materials (Basel). 2022;15:1978.

28. He JJ, Li DS, Jiang WG, Ke LM, Qin GH, Ye Y, et al. The martensitic transformation and mechanical properties of Ti6Al4V prepared via selective laser melting. Materials (Basel). 2019;12:321.

29. Guo JL, Shen YN. Several issues to pay attention to when calculating grain size using Scherrer's formula. Journal of Inner Mongolia Normal University. 2009;38:357-8.

30. Huang JG. Study of microstructure and properties of TC4 alloy by Selective Laser Melting. Nanchang: Nanchang Hangkong University; 2018. (in Chinese).

31. Toptan F, Alves AC, Carvalho Ó, Bartolomeu F, Pinto AMP, Silva F, et al. Corrosion and tribocorrosion behaviour of Ti6Al4V produced by selective laser melting and hot pressing in comparison with the commercial alloy. J Mater Process Technol. 2019;266:239-45.

32. Dai NW, Zhang LC, Zhang JX, Chen QM, Wu ML. Corrosion behavior of selective laser melted Ti6Al4V alloy in NaCl solution. Corros Sci. 2016;102:484-9.